

# Enabling pulsar and fast transient searches using coherent dedispersion

C. G. Bassa<sup>a</sup>, Z. Pleunis<sup>b</sup>, J. W. T. Hessels<sup>a,b</sup>

<sup>a</sup>*ASTRON, the Netherlands Institute for Radio Astronomy, Postbus 2, 7990 AA, Dwingeloo, The Netherlands*

<sup>b</sup>*Anton Pannekoek Institute for Astronomy, University of Amsterdam, Science Park 904, 1098 XH, Amsterdam, The Netherlands*

---

## Abstract

We present an implementation of the coherent dedispersion algorithm capable of dedispersing high-time-resolution radio observations to many different dispersion measures (DMs). This approach allows the removal of the dispersive effects of the interstellar medium and enables searches for pulsed emission from pulsars and other millisecond-duration transients at low observing frequencies and/or high DMs where time broadening of the signal due to dispersive smearing would otherwise severely reduce the sensitivity. The implementation, called `cdmt`, for *coherent dispersion measure trials*, exploits the parallel processing capability of general-purpose graphics processing units to accelerate the computations. We describe the coherent dedispersion algorithm and detail how `cdmt` implements the algorithm to efficiently compute many coherent DM trials. We present the concept of a semi-coherent dedispersion search, where coherently dedispersed trials at coarsely separated DMs are subsequently incoherently dedispersed at finer steps in DM. The software is used in an ongoing LOFAR pilot survey to test the feasibility of performing semi-coherent dedispersion searches for millisecond pulsars at 135 MHz. This pilot survey has led to the discovery of a radio millisecond pulsar – the first at these low frequencies. This is the first time that such a broad and comprehensive search in DM-space has been done using coherent dedispersion, and we argue that future low-frequency pulsar searches using this approach are both scientifically compelling and feasible. Finally, we compare the performance of `cdmt` with other available alternatives.

*Keywords:* methods: data analysis – pulsars: general

---

## 1. Introduction

Advances in electronics, computing and networking, primarily following Moore's law, have enabled the realization of a new type of radio telescope. Instead of placing receivers at the focus of movable reflecting dishes, these new telescopes employ a large number of stationary dipole antennas to create what is called an *aperture array*. The signals from these antennas are combined digitally in a correlator to create images of the sky, or in a beamformer to form beams on the sky. Three major digital aperture arrays operating at low radio frequencies are presently in operation: the LOW Frequency Array (LOFAR; van Haarlem et al. 2013), the Murchison Wide Field Array (MWA; Lonsdale et al. 2009; Tingay et al. 2013) and the Long Wavelength Array (LWA; Ellingson et al. 2009, 2013), while the low-frequency component of the Square Kilometre Array (SKA1-Low) is being planned (Braun et al., 2015). To maximize sensitivity while keeping the number of individual antennas, and hence cost, low, these aperture arrays operate at long wavelengths, and hence low observing frequencies (below 300 MHz).

One of the key science areas at these low observing frequencies is the study of radio pulsars. Radio emission from these highly magnetized, rotating neutron stars exhibits

a very steep spectrum (Maron et al., 2000; Bates et al., 2013), typically peaking or turning over between 100 to 200 MHz (e.g. Malofeev et al. 1994). Surveys at these low frequencies have the prospect of discovering new pulsars that are too faint to be detected in surveys performed at higher observing frequencies and can take advantage of large fields of view (e.g. Coenen et al. 2014). Of particular interest are radio pulsars spinning at millisecond spin periods. These millisecond pulsars provide unparalleled precision for measuring neutron star masses, performing precision tests of General Relativity, understanding binary evolution, and detecting gravitational waves (e.g. Kramer et al. 2006; Demorest et al. 2010; Ransom et al. 2014; Antoniadis et al. 2013; Verbiest et al. 2016).

Radio emission propagating through the ionized interstellar medium suffers from dispersion, introducing a frequency dependent time delay over the requisite large bandwidths of radio astronomical observations. As a result, pulsed signals, such as those of pulsars and fast transients (a generic term used for other sources of millisecond-duration radio pulses; e.g. Lorimer et al. 2007), have a specific dispersion measure (DM) which relates directly to the column density of free electrons between the source and the observer. When searching for new pulsars and fast transients, correcting for this dispersion is typically done through *incoherent dedispersion*, where the dispersive delays are removed by time shifting the time-series of

---

*Email address:* `bassa@astron.nl` (C. G. Bassa)

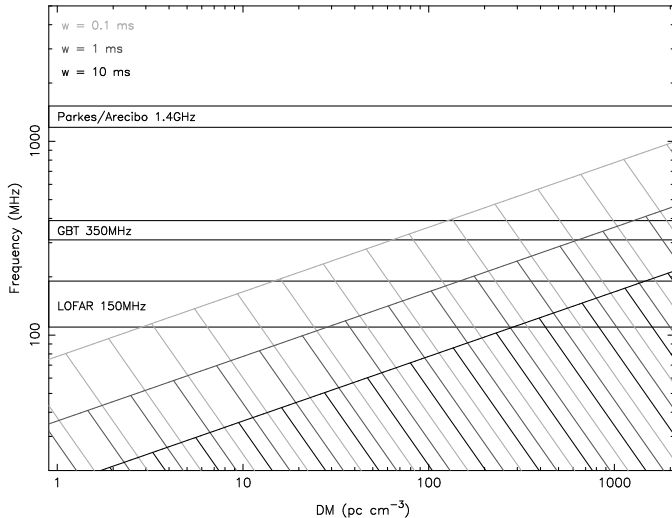


Figure 1: The effect of residual dispersion smearing in frequency channels as a function of dispersion measure (DM) and frequency. The diagonal lines denote the  $3\sigma$  detection limit of an undispersed input pulse of  $10\sigma$  with pulse full-width-half-maxima of  $w = 0.1$ , 1 and 10 ms. For frequencies below, or DMs above, these limits, denoted by the hashed areas, the pulse is no longer detectable. The channel size is set at  $\Delta\nu = 0.02$  MHz which corresponds to a time resolution of  $\Delta t = \Delta\nu^{-1} = 50 \mu\text{s}$ . This time resolution is what is typically used in current millisecond pulsar searches. Using narrower channels would adversely reduce the time resolution. The frequency bands and central frequencies of representative radio telescopes are shown with the horizontal lines.

individual, narrow, frequency channels by an amount appropriate to the DM of the source. Though this corrects for dispersion between channels, the dispersion within the finite bandwidth of the individual channels is not corrected for. Nonetheless, the computational efficiency of the technique has been a practical necessity compared to more accurate approaches.

A priori, the DM of a new pulsar or fast transient is unknown, and the data must be dedispersed to a broad range of different DMs. Models for the Galactic electron density (e.g. Cordes & Lazio 2002) can be used to estimate the maximum DM towards a given direction though – to enable sensitivity to extra-Galactic fast transients – most ongoing surveys search up to a maximum DM of several thousand  $\text{pc cm}^{-3}$ . Depending on the frequency and time resolution of the input data, several thousand DM trials may need to be computed (Cordes & McLaughlin, 2003)<sup>1</sup>. Though dedispersing that many DM trials is a computationally expensive task, recent implementations of incoherent dedispersion algorithms on graphics processing units (GPUs) are fast enough to allow real-time processing (Magro et al., 2011; Barsdell et al., 2012; Sclocco et al., 2016).

At low frequencies and/or high DMs, incoherent dedispersion can lead to significant smearing of the pulse (in

time) within a channel (see Fig. 1). The effect of dispersion can be completely removed though *coherent dedispersion*. This approach convolves the input signals with the inverse of the transfer function of the interstellar medium. This convolution must be performed before the signal is detected (squared) as the phase information, in addition to the amplitude, is required. Hence, the data rate and computational requirements for coherent dedispersion are typically larger than the filterbanked data used for incoherent dedispersion, as for the latter the two polarizations can be squared and frequency and/or time resolution can be reduced. Because of these higher data rates, coherent dedispersion is presently only used for observing either known pulsars or when searching for pulsars in globular clusters with known DMs.

Here we present *cdmt*, for *coherent dispersion measure trials*, which implements the coherent dedispersion algorithm to perform coherent dedispersion to many dispersion measure trials in parallel on GPUs. This software allows us to control the residual dispersion smearing within a channel and retain both high time and high frequency resolution when searching for pulsars and fast transients. In a semi-coherent dedispersion search, the input data can be coherently dedispersed to several coarsely separated trial DMs, each of which is then incoherently dedispersed with finer DM steps around the coherent trial DM. Though the total number of incoherent DM trials, and hence processing requirements, will increase, this approach allows us to search for millisecond pulsars at lower observing frequencies than were previously possible – thus probing a new astrophysical parameter space.

The paper is structured as follows. The coherent dedispersion algorithm, combined with channelizing the data, is described in § 2. Our implementation of the algorithm is outlined in § 3. In § 4 we provide an application example of the software and we report on the performance in § 5. Finally, we discuss prospects for *cdmt* in § 6.

## 2. Algorithm description

The coherent dedispersion algorithm as implemented in *cdmt* is that of a convolving synthetic filterbank. This implementation performs coherent dedispersion as a complex multiplication in the frequency domain and combines dedispersion with channelization. For a detailed description of the coherent dedispersion algorithm and different filterbanking versions, we refer to the implementation in the *dspsr* software package, which is detailed in van Straten & Bailes (2011)<sup>2</sup>. Here, we closely follow the description outlined in these references to explain our implementation. A schematic representation of the implementation is depicted in Figure 2.

Coherent dedispersion is a convolution of the raw signal voltages (Nyquist sampled time-series) with the inverse

<sup>1</sup>See Lyon et al. 2016 and <http://www.jb.man.ac.uk/pulsar/Surveys.html> for the parameters of ongoing and historic pulsar and fast transient surveys.

<sup>2</sup>See also Willem van Straten’s PhD thesis at <http://astronomy.swin.edu.au/~wvanstra/papers/thesis.html>

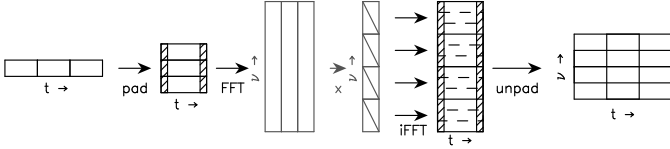


Figure 2: A schematic diagram depicting coherent dedispersion in a convolving synthetic filterbank. From left to right, the Nyquist sampled input time-series is broken up into sections of length  $N_{\text{bin}}$  (stage 1), which are overlapped by  $n_d n_c / 2$  time-samples at either end (stage 2). These sections are then Fourier transformed to the frequency domain (stage 3), and multiplied by the frequency domain transfer function of  $n_c$  channels (stage 4). A Fourier transform of length  $M_{\text{bin}} = N_{\text{bin}} / n_c$  back to the time domain is then performed for each channel to transform back to the time domain (stage 5). The overlap region of  $n_d$  time samples of each channelized time-series is then discarded (unpadded) to form the coherently dedispersed filterbank (stage 6). The black stages are in the time domain, the frequency domain stages are colored in gray.

of the transfer function of the interstellar medium (ISM). The convolution is most efficiently performed as a multiplication in the frequency domain through the discrete convolution theorem (see Press et al., 1992, Chapter 13.1). In addition to the convolution, the convolving synthetic filterbank trades time resolution for frequency resolution to create a user-defined number of channels  $n_c$  over the input bandwidth. This channelization step is combined with coherent dedispersion by performing a large forward Fourier transform of  $N_{\text{bin}}$  samples prior to dedispersion, followed by  $n_c$  backward Fourier transforms of  $N_{\text{bin}} / n_c$  samples to provide the channelization.

The transfer function of the ISM, when modelled as a cold tenuous plasma, is defined in the frequency domain (Hankins 1971; Hankins & Rickett 1975, see also Lorimer & Kramer 2012) as:

$$H(\nu + \nu_0) = \exp \left[ \frac{2\pi i \nu^2 k_{\text{DM}} \text{DM}}{\nu_0^2 (\nu + \nu_0)} \right]. \quad (1)$$

Here  $\nu_0$  is the center frequency of a subband or channel of bandwidth  $\Delta\nu$  (both in MHz), while  $\nu$  is the frequency offset within the channel or subband, such that  $-\Delta\nu/2 < \nu < \Delta\nu/2$ . The dispersion measure is DM (in  $\text{pc cm}^{-3}$ ) and  $k_{\text{DM}}^{-1} = 2.41 \times 10^{-4} \text{ s MHz}^2$  is a measured constant of proportionality (Manchester & Taylor, 1972). The duration of the transfer function is determined by the dispersion sweep  $t_d$  for the DM and parameters of the subband or channel ( $\nu_0, \Delta\nu$ ) being dedispersed,

$$t_d = k_{\text{DM}} (\nu_{\text{min}}^{-2} - \nu_{\text{max}}^{-2}) \text{DM}. \quad (2)$$

Here  $\nu_{\text{min}} = \nu_0 - \Delta\nu/2$  and  $\nu_{\text{max}} = \nu_0 + \Delta\nu/2$ . In `cdmt`, an input subband is channelized to  $n_c$  channels, each of which is coherently dedispersed with a transfer function (Eqn. 1) appropriate for that channel.

Owing to the underlying assumptions of the discrete convolution theorem, the edges of the output time-series will be polluted by the wrap around region. To prevent this, we use the *overlap-save* method, which requires each section of the time-series (raw signal voltages) of an input

subband to be overlapped by at least  $n_d n_c$  time samples (see van Straten & Bailes, 2011, Fig. 2 and 3). A total of  $n_d$  channelized time samples are subsequently discarded from the time-series of each output channel.

Given the sample rate  $r$  of the input subband, which is channelized to  $n_c$  output channels, the size of the overlap region is determined by  $n_d = r t_d / n_c$ . Here the dispersion sweep  $t_d$  is for the channel with the lowest frequency. The size  $N_{\text{bin}}$  of the forward Fourier transform can now be chosen such that  $N_{\text{bin}} > n_d n_c$ , while the  $n_c$  backward Fourier transforms have size  $M_{\text{bin}} = N_{\text{bin}} / n_c$ .

### 3. Implementation

Our aim was to develop software capable of efficiently computing synthetic filterbanks that are coherently dedispersed to many different DMs. To our knowledge, no such software currently exists. To accelerate the computations, we chose to perform the majority of the computations on many-core GPUs and develop our software using the NVIDIA Compute Unified Device Architecture (CUDA)<sup>3</sup> programming model. CUDA provides the `cuFFT` library<sup>4</sup>, which contains algorithms for performing large numbers of Fast Fourier Transforms (FFTs) in parallel on GPUs. Further acceleration was achieved by performing the majority of the computations in kernels that can be executed in parallel on the GPU. Intermediate results, such as reading the input data and performing the forward FFT, were reused to further boost efficiency. The implementation of the algorithm is given in Algorithm 1.

In the following, we will consider the input data to consist of  $n_s$  dual-polarization, complex-valued, Nyquist-sampled subbands. Each of these subbands will be channelized to  $n_c$  channels.

Initial processing steps consist of reading the metadata of the  $n_s$  input subbands, as well as initializing user-defined choices for the number of channels  $n_c$  per subband, the forward FFT size  $N_{\text{bin}}$ , and the size of the overlap region  $n_d$  appropriate for the input data. We have specifically chosen to keep  $N_{\text{bin}}$  and  $n_d$  identical for all subbands and channels. Though this reduces the efficiency of the algorithm, as more unpolluted time samples will be discarded, it also greatly reduces the complexity of the implementation, and allows multiple channels and subbands to be processed in parallel. Given the choices for  $N_{\text{bin}}$ ,  $n_c$  and  $n_d$  and the frequency setup of the input subbands, the transfer functions for each channel and each of the  $n_{\text{DM}}$  coherent DM trials are computed on the GPU.

The program then enters a loop where the input time-series of the subbands are read in blocks of  $N_{\text{FFT}}(N_{\text{bin}} - n_d n_c)$  time-samples at a time, which are copied to the GPU. The value for  $N_{\text{FFT}}$ , the number of FFTs performed in parallel, is chosen to maximize the usage of the GPU

<sup>3</sup>[http://www.nvidia.com/object/cuda\\_home\\_new.html](http://www.nvidia.com/object/cuda_home_new.html)

<sup>4</sup><http://developer.nvidia.com/cufft>

---

**Algorithm 1** cdmt pseudo algorithm

---

```
initialize (read metadata)
for idm = 0  $\rightarrow$  ndm do
  compute transfer function for DM[idm]
end for
for iblock = 0  $\rightarrow$  nblock do
  read block
  copy to device
  unpack, segment and pad
  forward FFT
  swap halves per subband
  for idm = 0  $\rightarrow$  ndm do
    complex multiplication with transfer function for
    DM[idm]
    swap halves per channel
    backward FFT
    transpose, unpad and detect
    compute block sums
    compute channel statistics
    redigitize
    copy to host
    write to disk
  end for
end for
```

---

memory. Once on the GPU, the input data blocks are unpacked into two `CUFFTComplex` arrays, one for each polarization. These data blocks are then segmented and padded to  $N_{\text{bin}}$  samples with an overlap region of  $n_d n_c / 2$  samples at each edge, forming a cube of  $N_{\text{bin}} N_{\text{FFT}} n_s$  samples for each polarization. These operations are performed in a single GPU kernel, where each axis of the cube maps directly onto the 3 dimensions of a grid of GPU thread blocks.

The `CUFFT` library is then used to perform two in-place, batch complex-to-complex forward FFTs of size  $N_{\text{bin}}$ , resulting in  $N_{\text{FFT}} n_s$  spectra of  $N_{\text{bin}}$  complex frequency bins each, one for each polarization. Since the output of the complex-to-complex FFT places the positive frequencies in the first half of the array and the negative frequencies in the second half, a GPU kernel swaps these halves around to arrange the frequency bins in increasing frequency.

Next, the program enters a second loop, this time over the  $N_{\text{DM}}$  different DM trials. In each iteration of this loop, the  $N_{\text{FFT}} n_s$  spectra of  $N_{\text{bin}}$  frequency bins for both polarizations are multiplied by the transfer functions of the  $n_c$  channels at the DM of that iteration. Since the transfer functions for different channels are consecutive, the complex multiplication creates  $N_{\text{FFT}} n_s n_c$  complex spectra of  $M_{\text{bin}} = N_{\text{bin}} / n_c$  frequency bins.

Before performing the backward FFT, the two halves of each spectrum of  $M_{\text{bin}}$  frequency bins are swapped back, using the same GPU kernel as before. The `CUFFT` library is again used to perform  $N_{\text{FFT}} n_s n_c$  complex-to-complex backward FFTs of size  $M_{\text{bin}}$  in batch mode for both polarizations. This transforms the coherently dedispersed

frequency bins back to the time domain.

The FFT output is now out of order, with the array indexes moving over time (data blocks), frequency (subbands), time (samples), and frequency (channels). A GPU kernel transposes the output to frequency (subbands and channels) to time (samples and data blocks). This transpose is combined with three further steps. First, it removes the effects of the padding step, where for each of the  $n_c$  channels of the  $n_s$  subbands for  $N_{\text{FFT}}$  blocks,  $n_d / 2$  time samples at each edge of the time-series are discarded. Secondly, the complex valued time-series of the two polarizations are squared and added to form Stokes I (intensity). Finally, the Stokes I output is packed such that spectra are in decreasing frequency order, forming a filterbank of  $N_{\text{FFT}}(M - n_d)$  spectra of  $n_s n_c$  channels.

At this stage it is beneficial to redigitize the floating point output to 8-bit integers to reduce data rates and disk storage. Data offsets and scales are computed from the average and standard deviation of the floating point time-series of each channel of  $N_{\text{FFT}}(M_{\text{bin}} - n_d)$  samples. To efficiently compute these offsets and scales for each channel, a GPU kernel first computes sums of intensity and intensity squared for segments of  $M$  samples in parallel. Next, another GPU kernel uses the sums for these segments to compute the average and standard deviation of each channel. A third GPU kernel then uses these values to determine the offset and scale of each channel, and use them to convert the floating point values to 8-bit integers. The  $N_{\text{FFT}}(M_{\text{bin}} - n_d) n_s n_c$  8 bit values for this data block and this coherent DM trial are copied back to the CPU and written to disk. The program then continues the loop over the coherent DM trials, and the loop over the data blocks until the entire input file has been processed.

#### 4. Application

The `cdmt` software was specifically designed for a survey with the LOFAR radio telescope (Stappers et al., 2011; van Haarlem et al., 2013) for millisecond pulsars associated with unidentified *Fermi*  $\gamma$ -ray sources from the 3FGL catalog (Acero et al., 2015). Here, we present results using the data from this survey as input; the full scientific results of the survey will be presented in a forthcoming paper (Pleunis et al., in prep.).

The LOFAR survey targeted 52 so-called ‘unidentified’ *Fermi*  $\gamma$ -ray sources with the LOFAR HBAs (high band antennas). These are sources of  $\gamma$ -ray emission, identified with the *Fermi Gamma-ray Space Telescope*, for which the astrophysical origin of the emission is still unclear. Pulsars are one of the prime candidates for creating such emission, and radio pulsation searches towards these  $\gamma$ -ray sources can provide a definitive identification, as well as the basis for further scientific insights.

Each source was observed for 20 min, and the LOFAR COBALT correlator formed 7 tied-array beams<sup>5</sup> to cover

---

<sup>5</sup>A tied-array beam can be considered as a field of view on the sky

the error regions of the  $\gamma$ -ray sources. For each of these tied-array beams, 200 dual-polarization, complex valued, Nyquist sampled subbands of 195.31 kHz (39.06 MHz total) bandwidth, centered at a frequency of 135 MHz, were recorded to disk. The observations were processed on the DRAGNET GPU cluster, which consists of 23 nodes, each of which has 4 NVIDIA Titan X GPUs, 128 GB of RAM and dual 8-core Xeon E5-2630 CPUs. The nodes are interconnected with 1 Gb and 10 Gb ethernet networks. The observations were stored on 20 of the 23 nodes, with the bandwidth of each source distributed over 20 parts of 10 consecutive subbands each, with one part stored on each node.

Since the survey specifically targets sources at high Galactic latitudes, the maximum DM was chosen at  $80 \text{ pc cm}^{-3}$ , which is approximately twice the maximum DM predicted by the NE2001 Galactic electron density model (Cordes & Lazio, 2002) towards the selected *Fermi*  $\gamma$ -ray sources. The 195.31-kHz subbands were channelized to  $n_c = 8$  channels of 24.41 kHz, yielding a time resolution of  $40.96 \mu\text{s}$ . No further averaging in frequency or time was performed. We chose to limit the effects of dispersive smearing to less than 0.07 ms, and to allow at least 10 independent pulse phase bins for a millisecond pulsar with a spin period of 1 ms. To achieve this, we used `cdmt` to coherently dedisperse these observations over 80 coherent DM trials. These DM trials were spaced at  $1 \text{ pc cm}^{-3}$  from  $0.5 \text{ pc cm}^{-3}$  to  $79.5 \text{ pc cm}^{-3}$ . Figure 3 shows the dispersive smearing for the observational setup and semi-coherent dedispersion approach. The size of the forward FFT was chosen at  $N_{\text{bin}} = 65536$  samples, with an overlap region of  $n_d = 2048$  samples (with  $n_c = 8$ ,  $M_{\text{bin}} = 8192$  samples). The available memory on the NVIDIA Titan X GPU allowed  $N_{\text{FFT}} = 100$  FFTs of  $N_{\text{bin}}$  samples to be coherently dedispersed in parallel.

Each of the coherently dedispersed filterbanks was then incoherently dedispersed at steps of  $0.002 \text{ pc cm}^{-3}$  ranging from  $-0.5$  to  $0.5 \text{ pc cm}^{-3}$  around the coherently dedispersed DM of the filterbank data set. Here, we used the GPU accelerated brute force dedispersion algorithm from the DEDISP<sup>6</sup> library by Barsdell et al. (2012) to generate incoherently dedispersed time-series. Further processing was performed with programs from the PRESTO suite of pulsar search software<sup>7</sup> (Ransom, 2001). In particular, power spectra for each incoherently dedispersed time-series were created with `realfft`, and then searched for Doppler-shifted periodic signals through a frequency-domain acceleration search with a GPU-accelerated version of PRESTO's `accelsearch`<sup>8</sup> (Ransom et al., 2002). Finally, pulsar candidates were folded and their parameters (spin period, DM and acceleration) optimized with `prepfold`.

obtained by coherently adding the signals from individual LOFAR stations using appropriate time and phase delays.

<sup>6</sup><http://code.google.com/archive/p/dedisp/>

<sup>7</sup><http://github.com/scottransom/presto>

<sup>8</sup>[http://github.com/jintaolu/presto\\_on\\_gpu](http://github.com/jintaolu/presto_on_gpu)

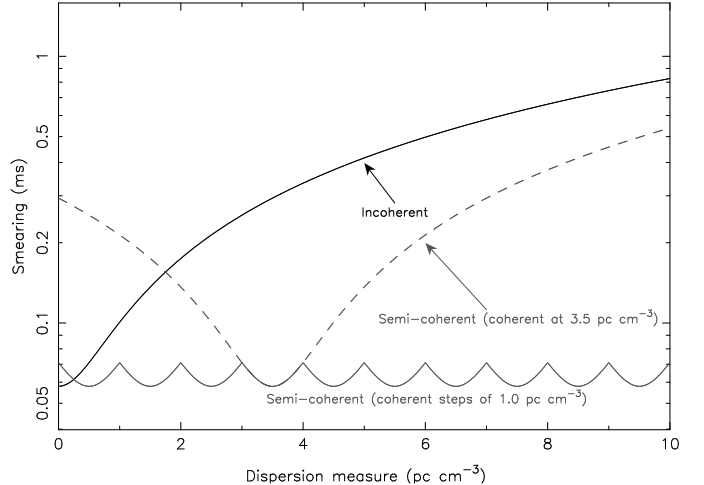


Figure 3: Smearing due to the combined effects of dispersion within a channel, finite time resolution, and finite DM steps over the full bandwidth, as a function of DM. The survey parameters are as described in the text. A fully incoherent dedispersion approach is shown with the solid black line. The smearing quickly exceeds 0.1 ms for DMs larger than  $1 \text{ pc cm}^{-3}$ . Using a semi-coherent dedispersion approach, first coherently dedispersing the data to a DM of  $3.5 \text{ pc cm}^{-3}$  and then using incoherent dedispersion, results in the dashed gray line, which is a horizontally shifted copy of the black line. Here, the smearing is below 0.1 ms between a DM of 2.5 and  $4.5 \text{ pc cm}^{-3}$ . Using coherently dedispersed data at steps of  $1 \text{ pc cm}^{-3}$ , and then incoherently dedispersing in between, results in the solid gray line; limiting the dispersive smearing to less than 0.07 ms.

The `cdmt` coherent dedispersion algorithm and the pulsar search pipeline were tested on observations of pulsars J1810+1744 and J2215+5135, which are binary radio millisecond pulsars visible at radio frequencies of 150 MHz (Kondratiev et al., 2016). Both pulsars were blindly re-discovered through the pipeline described above. Figure 4 shows integrated pulse profiles as well as pulse phase as a function of time for both millisecond pulsars. For both pulsars coherent dedispersion is required, as the dispersion smearing within a 24-kHz channel at a frequency of 135 MHz exceeds the pulsar spin period  $P$ ; for PSR J1810+1744, the smearing at  $\text{DM} = 39.658 \text{ pc cm}^{-3}$  is  $t_d = 3.3 \text{ ms}$ , while the spin period is  $P = 1.66 \text{ ms}$ , while PSR J2215+5135 has  $P = 2.61 \text{ ms}$  with  $t_d = 5.7 \text{ ms}$  at  $\text{DM} = 69.194 \text{ pc cm}^{-3}$ .

While preparing this manuscript, a new radio millisecond pulsar was discovered as part of the LOFAR survey for *Fermi*  $\gamma$ -ray sources. It has  $P = 2.43 \text{ ms}$  at a  $\text{DM} = 22.901 \text{ pc cm}^{-3}$ . This discovery and the full description of the survey will be published elsewhere (Pleunis et al., in prep.).

## 5. Performance

With the dataset as described in §4 as input, we can test the performance of `cdmt`. Here we specifically focus on subbands with the lowest observing frequencies, where the DM delays are largest. In particular, the input data

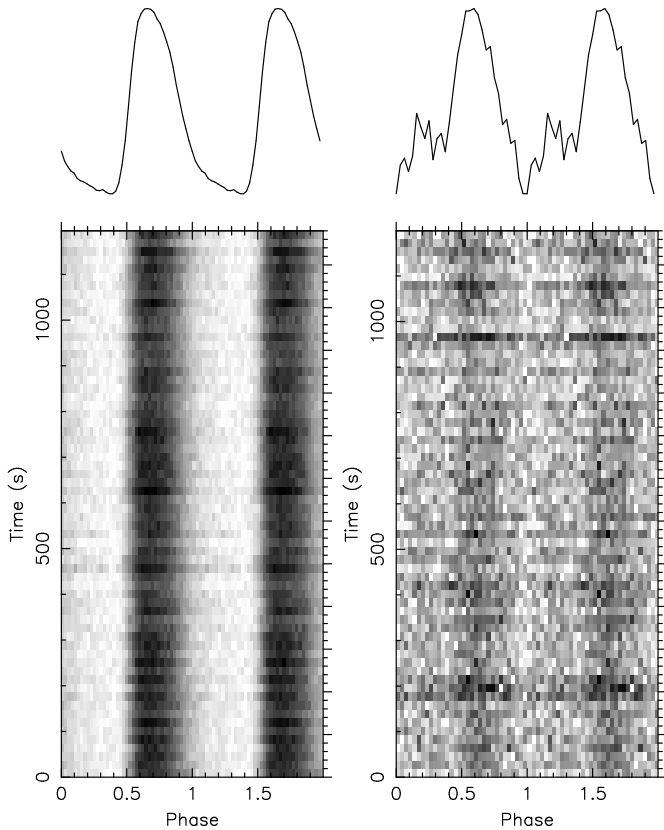


Figure 4: Integrated pulse profiles (top curves; two full cycles are shown for clarity) and pulse brightness as a function of time (bottom panel) for test observations of PSR J1810+1744 (left) and PSR J2215+5135 (right). These are 20-min observations with the LOFAR HBA of 39 MHz of bandwidth centered on 135 MHz. PSR J1810+1744 has  $P = 1.66$  ms and  $DM = 39.658$  pc cm $^{-3}$  and PSR J2215+5135 has  $P = 2.61$  ms and  $DM = 69.194$  pc cm $^{-3}$ . Both pulsars were blindly redetected using the semi-coherent dedispersion pipeline presented here.

consists of one part with 10 consecutive subbands with frequencies between 114.93 and 116.88 MHz. The performance of `cdmt` on a DRAGNET node using a single NVIDIA Titan X GPU is shown in Fig. 6. Here, we use the following parameters;  $N_{\text{bin}} = 65536$  samples,  $n_d = 2048$  samples,  $n_c = 8$  output channels per subband and  $N_{\text{FFT}} = 100$  FFTs processed in parallel. Besides the processing time of all steps in `cdmt`, we also show the processing time in the absence of reading from and writing data to disk. Here the processing time is set by the remaining steps (primarily the GPU operations; CUDA memory copies, `CUFFT` operations and CUDA kernel operations). As expected, we find that the GPU operations scale linearly with the number  $N_{\text{DM}}$  of DM trials that are coherently dedispersed, but that disk operations limit the performance. The input data is 8.8 GB while for each DM trial 2.2 GB of output needs to be written to disk.

Besides `cdmt`, coherently dedispersing a single DM is possible with the `digifil` software. This program is part

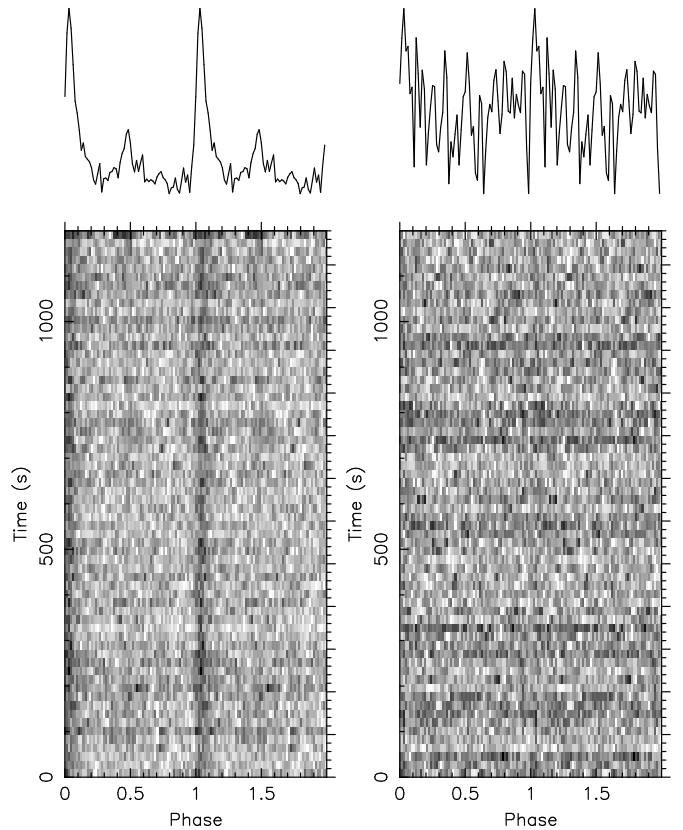


Figure 5: Same as Fig. 4 but now for the 20-min discovery observation of PSR J1552+54. The left panel shows the result of coherently dedispersing the data at a  $DM = 22.5$  pc cm $^{-3}$ , and then using incoherent dedispersion at the DM of the pulsar ( $DM = 22.901$  pc cm $^{-3}$ ). The right panel shows the same pulse profile when using incoherent dedispersion only. The pulse profile is no longer significant due to dispersive smearing within each of the 24-kHz channels.

of the `DSPSR`<sup>9</sup> software package (van Straten & Bailes, 2011) and performs coherent dedispersion on CPUs. In Fig. 6 we also provide the processing time of `digifil` for the same input dataset on a Xeon E5-2630 CPU using 1, 2 or 4 CPU threads. We find that for coherently dedispersing a single dispersion measure on the DRAGNET hardware, the performance of `cdmt` is comparable to running `digifil` with 4 threads. Like `cdmt`, the performance of `digifil` is limited by disk operations, as using more than 4 threads does not decrease the processing time. When coherently dedispersing multiple DM trials, `cdmt` will significantly outperform `digifil` due to the data reuse in `cdmt`. We do note that `digifil` optimizes the choice for FFT size  $N_{\text{bin}}$  and data overlap  $n_d$  depending on the DM and observing frequency of the actual input data. As a result, `digifil` will be somewhat more efficient at low DMs and/or higher observing frequencies compared to the fixed  $N_{\text{bin}}$  and  $n_d$  values used by `cdmt` that are chosen for the lowest observing frequency of the input data and highest DM required for the particular project.

The use of semi-coherent dedispersion offers higher time

<sup>9</sup><http://dspsr.sourceforge.net>

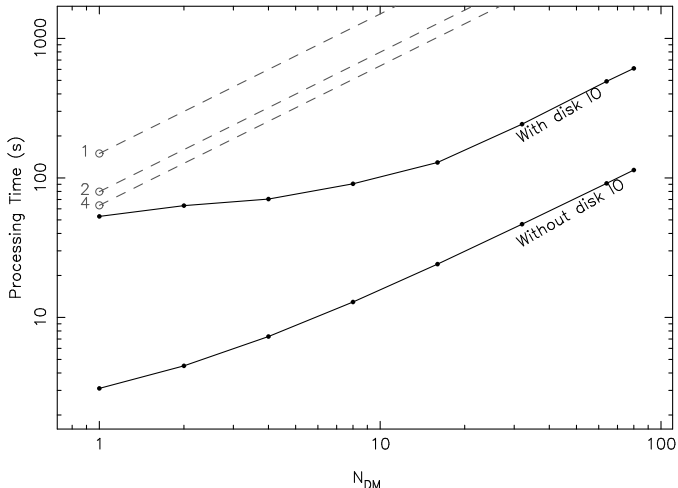


Figure 6: Performance of `cdmt` as a function of the number of coherently dedispersed DM trials. The input data consists of a 20-min observation with 10 consecutive dual-polarization, complex valued, Nyquist sampled subbands of 195.31 kHz bandwidth with frequencies between 114.93 and 116.88 MHz. These are the lowest-frequency subbands from the LOFAR survey. An NVIDIA Titan X GPU was used with  $N_{\text{bin}} = 65536$  samples,  $n_d = 2048$  samples,  $n_c = 8$  output channels per subband and  $N_{\text{FFT}} = 100$  FFTs processed in parallel. The top curve shows the `cdmt` performance when reading in 8.8 GB of input data and writing 2.2 GB of output data per DM trial. The bottom curve shows the `cdmt` performance when removing the disk reading and writing operations (CUDA memory copies, cuFFT operations and CUDA kernel operations). For comparison, the performance of `digifil` (van Straten & Bailes, 2011) for single or multi-threaded operation (1, 2 or 4 CPUs) on an 8-core Xeon E5-2630 CPU is shown with the gray open circles. Here, `digifil` computes a single DM trial. The extrapolated performance of `digifil` when coherently dedispersing multiple DM trials sequentially is shown with the dashed lines. Each point here is the average processing time of 10 runs.

resolution at all DMs, though requires having to perform more incoherent DM trials. The semi-coherent dedispersion approach used for the LOFAR *Fermi*  $\gamma$ -ray source survey limits the dispersion smearing to 0.07 ms. Hence the time resolution and DM step size for incoherent dedispersion can remain at 40.96  $\mu\text{s}$  and 0.002  $\text{pc cm}^{-3}$  over the full DM range. As a result, 40,000 incoherent DM trials are required. For comparison, using the PRESTO dedispersion planning tool `DDp1an.py`, a fully incoherent search up to a maximum DM of 80  $\text{pc cm}^{-3}$  would require only 7,240 incoherent DM trials. However, without coherent dedispersion the time and frequency resolution would have no sensitivity for millisecond pulsars with periods below 10 ms at DMs above 10  $\text{pc cm}^{-3}$  (see Fig. 3).

## 6. Discussion

Correcting for dispersion in surveys for pulsars and FRBs through incoherent dedispersion is no longer a major computational bottleneck. Recent implementations of incoherent dedispersion algorithms on GPUs are fast enough to allow real-time processing (Magro et al., 2011; Barsdell et al., 2012; Sclocco et al., 2016). We have presented `cdmt`,

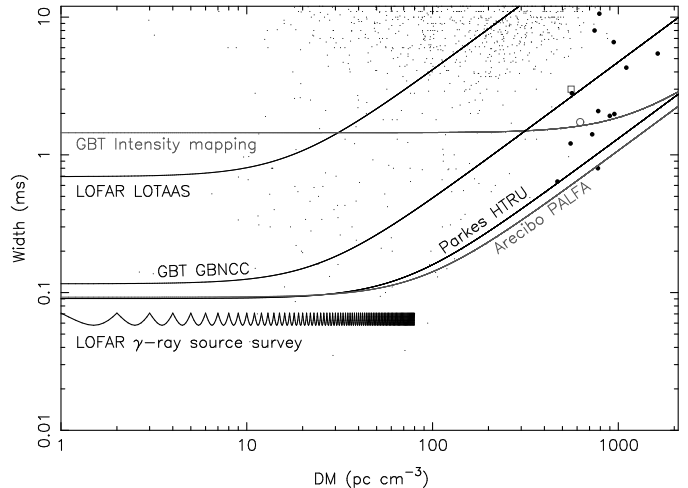


Figure 7: The DM and pulse width of pulsars (small dots) and Fast Radio Bursts (FRBs) discovered by the Parkes (large dots), Arecibo (open square) and GBT (open circle) radio telescopes. Pulsar parameters have been taken from the pulsar catalogue (Manchester et al., 2005), while FRB parameters originate from the FRB catalogue (Petroff et al., 2016). Pulse broadening curves for ongoing pulsar surveys with the Parkes (HTRU, 1.4 GHz; Keith et al. 2010), Arecibo (PALFA, 1.4 GHz; Lazarus et al. 2015), GBT (GBNCC, 350 MHz; Stovall et al. 2014) and LOFAR (LOTAAS, 135 MHz; Coenen et al. 2014) radio telescopes are shown with solid lines. Also shown is the broadening curve for a Hydrogen intensity mapping experiment with the GBT (800 MHz), which discovered an FRB (open circle, Masui et al. 2015). The pulse broadening takes into account finite sampling times and dispersion smearing within channels, though neglects the effects of scattering. All surveys use incoherent dedispersion, except for the LOFAR *Fermi*  $\gamma$ -ray source survey described in this paper. By combining coherent and incoherent dedispersion, this survey limits pulse broadening over the entire DM range that is being surveyed.

the next step in correcting for dispersion; an implementation to perform coherent dedispersion for many different DM trials. These DM trials serve as input for further incoherent dedispersion and allow semi-coherent dedispersion searches for pulsars and FRBs. The combination of coherent and incoherent dedispersion limits the dispersion smearing and allows a more flexible choice of channel size and sampling time at different observing frequencies and dispersion measures.

We are using `cdmt` in an ongoing LOFAR survey of radio millisecond pulsars associated with unidentified *Fermi*  $\gamma$ -ray sources. With this approach, we limit the dispersion smearing at these low observing frequencies over the DM range being surveyed, retaining sensitivity to short period pulsars at all DMs being sampled (see Fig. 7). The success of this approach has already been demonstrated with the discovery of a new millisecond pulsar (Fig. 5).

Surveys for pulsars and fast transients are key science goals for SKA1-Low and SKA1-Mid (Hessels et al., 2015; Keane et al., 2015; Macquart et al., 2015). Though the use of semi-coherent dedispersion is currently not planned, the SKA1-Low survey for pulsars at high Galactic latitudes can benefit from this approach. As the SKA1-Low pulsar survey will likely operate at higher frequencies (200

to 350 MHz; Keane et al. 2015) in comparison to LOFAR, dispersion smearing will be lower and hence fewer coherent DM trials would be required. For an example setup of 100 MHz of bandwidth at a center frequency of 250 MHz, a time resolution of 50  $\mu$ s and 20 kHz channels, coherently dedispersed DM step sizes of 10 pc cm<sup>-3</sup> would provide a maximum dispersion smearing of 90  $\mu$ s.

Semi-coherent dedispersion searches may also be useful at higher observing frequencies. Recent FRB discoveries at observing frequencies of 1.4 GHz have DMs in excess of 1,000 pc cm<sup>-3</sup> (Thornton et al., 2013; Champion et al., 2016; Petroff et al., 2016) and for these the width of the pulses is dominated by dispersion smearing within a channel (Fig. 7). Coherently dedispersing to a few DM trials spaced at intervals of 10 to 100 pc cm<sup>-3</sup> would keep the pulse broadening due to dispersion smearing below 0.1 ms and increase the signal to noise of detected pulses, while also giving a more accurate portrayal of the intrinsic pulse duration.

The `cdmt` software is continuing development, with new features being planned. Features being worked on include implementing the spectral kurtosis method (Nita & Gary, 2010a,b), in order to reject radio frequency interference when computing data offsets and scales to remove its influence on the redigitization, and reading and writing different input and output formats. The code is publicly available at <http://github.com/cbassa/cdmt>.

## Acknowledgments

We thank Vlad Kondratiev, Sotiris Sanidas and Alexander van Amesfoort for their contributions to the design and construction of the DRAGNET computing cluster, as well as comments on drafts of this manuscript. The research leading to these results has received funding from the European Research Council under the European Union’s Seventh Framework Programme (FP7/2007-2013) / ERC grant agreement nr. 337062 (DRAGNET; PI Hessels).

## References

Acero F., et al., 2015, *ApJS*, **218**, 23  
 Antoniadis J., et al., 2013, *Science*, **340**, 448  
 Barsdell B. R., Bailes M., Barnes D. G., Fluke C. J., 2012, *MNRAS*, **422**, 379  
 Bates S. D., Lorimer D. R., Verbiest J. P. W., 2013, *MNRAS*, **431**, 1352  
 Braun R., Bourke T., Green J. A., Keane E., Wagg J., 2015, *Advancing Astrophysics with the Square Kilometre Array (AASKA14)*, p. 174  
 Champion D. J., et al., 2016, *MNRAS*,  
 Coenen T., et al., 2014, *A&A*, **570**, A60  
 Cordes J. M., Lazio T. J. W., 2002, preprint, ([arXiv:0207156](https://arxiv.org/abs/0207156))  
 Cordes J. M., McLaughlin M. A., 2003, *ApJ*, **596**, 1142  
 Demorest P. B., Pennucci T., Ransom S. M., Roberts M. S. E., Hessels J. W. T., 2010, *Nat*, **467**, 1081  
 Ellingson S. W., Clarke T. E., Cohen A., Craig J., Kassim N. E., Pihlstrom Y., Rickard L. J., Taylor G. B., 2009, *IEEE Proceedings*, **97**, 1421  
 Ellingson S. W., et al., 2013, *IEEE Transactions on Antennas and Propagation*, **61**, 2540

Hankins T. H., 1971, *ApJ*, **169**, 487  
 Hankins T. H., Rickett B. J., 1975, *Methods in Computational Physics*, **14**, 55  
 Hessels J., et al., 2015, *Advancing Astrophysics with the Square Kilometre Array (AASKA14)*, p. 47  
 Keane E., et al., 2015, *Advancing Astrophysics with the Square Kilometre Array (AASKA14)*, p. 40  
 Keith M. J., et al., 2010, *MNRAS*, **409**, 619  
 Kondratiev V. I., et al., 2016, *A&A*, **585**, A128  
 Kramer M., et al., 2006, *Science*, **314**, 97  
 Lazarus P., et al., 2015, *ApJ*, **812**, 81  
 Lonsdale C. J., et al., 2009, *IEEE Proceedings*, **97**, 1497  
 Lorimer D. R., Kramer M., 2012, *Handbook of Pulsar Astronomy*  
 Lorimer D. R., Bailes M., McLaughlin M. A., Narkevic D. J., Crawford F., 2007, *Science*, **318**, 777  
 Lyon R. J., Stappers B. W., Cooper S., Brooke J. M., Knowles J. D., 2016, *MNRAS*,  
 Macquart J. P., et al., 2015, *Advancing Astrophysics with the Square Kilometre Array (AASKA14)*, p. 55  
 Magro A., Karastergiou A., Salvini S., Mort B., Dulwich F., Zarb Adami K., 2011, *MNRAS*, **417**, 2642  
 Malofeev V. M., Gil J. A., Jessner A., Malov I. F., Seiradakis J. H., Sieber W., Wielebinski R., 1994, *A&A*, **285**  
 Manchester R. N., Taylor J. H., 1972, *ApJ*, **10**, 67  
 Manchester R. N., Hobbs G. B., Teoh A., Hobbs M., 2005, *AJ*, **129**, 1993  
 Maron O., Kijak J., Kramer M., Wielebinski R., 2000, *A&AS*, **147**, 195  
 Masui K., et al., 2015, *Nat*, **528**, 523  
 Nita G. M., Gary D. E., 2010a, *PASP*, **122**, 595  
 Nita G. M., Gary D. E., 2010b, *MNRAS*, **406**, L60  
 Petroff E., et al., 2016, preprint, ([arXiv:1601.03547](https://arxiv.org/abs/1601.03547))  
 Press W. H., Teukolsky S. A., Vetterling W. T., Flannery B. P., 1992, *Numerical recipes: The art of scientific computing*. Cambridge: University Press, 2nd ed.  
 Ransom S. M., 2001, PhD thesis, Harvard University  
 Ransom S. M., Eikenberry S. S., Middleditch J., 2002, *AJ*, **124**, 1788  
 Ransom S. M., et al., 2014, *Nat*, **505**, 520  
 Sclocco A., van Leeuwen J., Bal H. E., van Nieuwpoort R. V., 2016, *Astronomy and Computing*, **14**, 1  
 Stappers B. W., et al., 2011, *A&A*, **530**, A80  
 Stovall K., et al., 2014, *ApJ*, **791**, 67  
 Thornton D., et al., 2013, *Science*, **341**, 53  
 Tingay S. J., et al., 2013, *Proc. Astr. Soc. Aust.*, **30**, e007  
 Verbiest J. P. W., et al., 2016, *MNRAS*, **458**, 1267  
 van Haarlem M. P., et al., 2013, *A&A*, **556**, A2  
 van Straten W., Bailes M., 2011, *Proc. Astr. Soc. Aust.*, **28**, 1